Supporting Information for:

Multi-Scale Simulations of Excited-State Energy Transfer Pathways in the C_2S_2-Type PSII-LHCII Supercomplex of Spinach

Jianping Guo[1], Fan Xu[1], Ruichao Mao[1, 2], Lihua Bie[1], Luning Liu[1, 3], Jun Gao[1]*

[1] Hubei Key Laboratory of Agricultural Bioinformatics, College of Informatics, Huazhong Agricultural University, Wuhan 430070, China
[2] College of Chemical and Biological Engineering, Zhejiang University, Hangzhou 310058, China
[3] Institute of Systems, Molecular and Integrative Biology, University of Liverpool, Liverpool L69 7ZB, UK

*Corresponding author: gaojun@mail.hzau.edu.cn

METHODS

Spectral simulation

The absorption spectrum was computed by averaging over an ensemble of 20 representative snapshots extracted from the molecular dynamics trajectory. For each snapshot, site energies and inter-pigment couplings derived from QM/MM calculations were utilized to simulate the spectral line shape. The calculated spectra were broadened using a Gaussian window to model inhomogeneous broadening effects[1].

$$A(\nu) = \frac{\nu}{2\sqrt{\pi}\sigma}\sum_{i=1}^{206} M_i^2 exp\left[-\frac{(h\nu - \varepsilon_I - \Delta E)^2}{2\sigma^2}\right]$$

Gaussian broadening with a standard deviation of σ=0.012 eV was applied. To align the calculated spectrum with the experimental Q_y band position, a global energy shift of ΔE=-0.285 eV was introduced, compensating for the systematic overestimation of excitation energies by the CAM-B3LYP functional. The final theoretical spectrum was obtained by averaging the individually broadened spectra and compared with the experimental room-temperature absorption spectrum of the PSII-LHCII supercomplex reported by Wei et al[2].

Linear Optical Spectra

The linear spectra of the isolated CP43 antenna were calculated according to the methodology developed by the Thomas Renger group in their spectroscopic simulations[3-6]. In this work, the CP43 subcomplex is treated as a separate excitonic domain. The absorption spectrum was computed as

$$\alpha(\omega) = \omega \sum_{M_d} \left|\mu_{M_d}\right|^2 D_{M_d}(\omega)$$

where the transition dipole moment is given by

$$\vec{\mu}_{M_d} = \sum_{m_d} c_{m_d}^{(M_d)} \vec{\mu}_{m_d}$$

With $\vec{\mu}_{m_d}$ being the local transition dipole moment of pigment m_d Each spectrum was broadened using a Gaussian lineshape function with a full width at half maximum (FWHM) of 180 cm^{-1}.

For the linear dichroism (LD) spectrum, the quantity $\left|\mu_{M_d}\right|^2$ in the absorption expression is replaced by

$$\left|\mu_{M_d}\right|^2 \left(1 - 3\cos\left(\theta_{M_d}\right)^2\right)$$

Where θ_{M_d} is the angle between the transition dipole and a chosen reference axis (Z axis).

For the circular dichroism (CD) spectrum, the rotational strength of exciton state M_d is used:

$$r_{M_d} = \sum_{m_d > n_d} c_{m_d}^{(M_d)} c_{n_d}^{(M_d)} \vec{R}_{m_d n_d} \cdot \vec{\mu}_{m_d} \times \vec{\mu}_{n_d}$$

All site energies and inter-pigment electronic couplings were taken directly from the multiscale calculations performed on the complete PSII-LHCII supercomplex, as described in the main text. The final spectra presented in this study were obtained by averaging the results computed from an ensemble of representative structural frames.

RESULTS AND DISCUSSION

Spectral fitting analysis

Compared to the experimental room-temperature absorption spectra[2, 7], the theoretically averaged absorption spectrum reproduces several key spectral features (Fig. S3). Specifically, the main chlorophyll a peak is located at 675 nm, matching the experimental peak position (675 nm). In contrast, the chlorophyll b-related peak appears at 626 nm, showing a distinct blue shift relative to the experimental value of 650 nm, with a deviation of approximately 24 nm. Although averaging over multiple configurations brings the theoretical spectrum closer to the experimental one, a systematic deviation remains for the chlorophyll b-related band.

In subsequent calculations of energy transfer rates based on Förster theory, the experimental peak positions (Chl a: 675 nm; Chl b: 650 nm)[2, 7] were directly used in the spectral overlap computation for energy transfer between different types of pigments (e.g., Chl b → Chl a). This ensures that the donor–acceptor energy gap aligns with the experimentally observed absorption bands. At the same time, for energy transfer between pigments of the same type (e.g., Chl a → Chl a, Chl b → Chl b), the rates were still evaluated using the spectral overlap derived from the theoretically computed site energies and corresponding line shapes. This approach maintains the internal consistency and transferability of the theoretical model. Such a treatment strictly aligns the energy matching between different types of pigments with the experimental spectral peaks without altering the previously validated coupling and broadening parameters, thereby improving the quantitative reliability of the relevant energy transfer pathways. It also preserves the theoretical sensitivity of same-type pigment pathways to microenvironment perturbations and configurational fluctuations, facilitating further analysis within the homogeneous pigment network.

Overall, the averaged spectrum shows good agreement with the experimental spectrum at the main chlorophyll a peak, while the shift in the chlorophyll b-related band has been explicitly corrected in the rate calculations via the described spectral overlap strategy, laying a solid foundation for subsequent theoretical modeling of energy transfer.

The critical role of donor-acceptor distance in EET

The inter-pigment distances and energy transfer rates for key pathways between the peripheral and inner antennas were identified (Fig. S4, Table S3). Distances were measured as the Mg–Mg distance between chlorophylls. As summarized in Table S3, the forward and backward transfer rates for a given pigment pair differ owing to their site energy differences. Nonetheless, both the data and the figure clearly demonstrate that fast energy transfer requires a short spatial separation as a fundamental condition.

According to Förster theory, the energy transfer rate is governed by the product of the distance-dependent electronic coupling and the site energy-dependent spectral overlap. To elucidate the fundamental role of distance, we plotted the electronic coupling strength against the inter-pigment distance for all pairs within 100 Å (Fig. S5). The results reveal a sharp decay in electronic coupling with increasing distance, confirming that distance sets the upper limit of the energy transfer rate between any two pigments. Notably, substantial variations in coupling

strength were observed even at similar distances, arising primarily from differences in the relative orientation between pigments. This is illustrated by the example of pigments a605, a613, and a614 in CP43 (Fig. S5). Although the distance between a614 and a605 is only 8.8 Å, their coupling remains weak (4.1 cm^{-1}). In contrast, the a614-a613 pair, with a distance of 9.1 Å, exhibits a coupling of 64.4 cm^{-1}, due to their more parallel orientation.

In summary, the directionality and specificity of the energy transfer network in our study emerge from the synergy between the spatial architecture (distance and orientation) and the energy landscape: the former defines the potential channels for energy flow, while the latter provides the net driving force through these channels.

Probing the role of the energy gradient by imposing uniform site energies

To probe the functional role of the intrinsic energy landscape, we set all pigment site energies to an equal value (675 nm) and recalculated the energy transfer rates. This manipulation fundamentally altered the nature of excitation energy flow. The removal of the energy gradient eliminated directional driving forces, resulting in identical forward and backward transfer rates between pigment pairs and leading to random energy diffusion without net directionality. Although the overall connectivity of the energy transfer network was preserved, its dynamics were significantly perturbed. For example, the fast, directional pathway from a612 in LHCII M1 to a506 in CP43, observed in the native system (Fig. 4), was converted into a bidirectional and rapid exchange under the equal-energy condition (Fig. S6). Furthermore, the transfer times for most original pathways increased, while new channels, such as those involving chlorophyll b sites, emerged (Table S4).

At the subunit level, the uniform energy landscape drastically reshapes the energy funnelling pattern. Generalized Förster calculations revealed rapid mutual energy exchange between peripheral antennas (e.g., between CP26 and LHCII), with excitation becoming trapped within the peripheral regions and even accumulating preferentially in LHCII, rather than being directed inward to the core antennas (Fig. S7). A key finding was the significant slowdown in energy transfer from LHCII to CP43, with the time constant increasing from 19 ps to 49 ps (Fig. S7), confirming that the absence of an energy gradient severely compromises energy funnelling toward the reaction center. However, the time constants for the transfer of CP43 and CP47 to RC were reduced.

The loss of directionality was also evident at the level of individual subunits. Analysis of excitation energy transfer dynamics within CP43 showed that under the native energy landscape, energy rapidly funnels from a504 to the low-energy trap sites a505 and a501 (Fig. S8). In contrast, under equal site energies, energy diffused randomly to all neighboring sites after initial excitation at a504, with no effective funnelling observed (Fig. S9). The EET dynamics were modeled by employing a master equation approach[8].

In conclusion, this control experiment demonstrates that heterogeneous site energies are essential for establishing a directional energy transfer network.

Calculated and literature site energies

This study obtained the site energies of pigments in the PSII-LHCII supercomplex through multiscale QM/MM calculations, which incorporate the effects of the protein environment. The results are presented as averages over representative conformations (a uniform energy shift of -0.285 eV has been applied). This work also compiles site energy data selected from prior studies[3-5, 9-15], which were typically derived from fitting spectroscopic data to subunit-level models. All values are listed in eV (Table S5-S9).

The site energies calculated in this study generally fall within the range reported in prior work[9-11]. However, a difference is observed for the "special pair" in the reaction center. In prior work, such as the parameter set established by Raszewski et al., assigned identical site energies (1.862 eV) to the P_{D1} and P_{D2} chlorophylls[4], treating them as a symmetric "special pair". Our calculations yield distinct site energies for P_{D1} and P_{D2}, suggesting that within the intact PSII-LHCII supercomplex, they may not constitute a conventional symmetric special pair. This result aligns with the view proposed by Saito et al., who described them as behaving more like independent monomers[16]. The difference likely stems from the fact that our calculations are based directly on the full PSII-LHCII structure, unlike previous parameterizations derived from isolated subunits.

Comparison of calculated and experimental linear spectra for the CP43

As shown in Fig. S10, the calculated absorption spectrum of CP43 at room temperature is consistent with the corresponding experimental data[6] (293 K) in the 650–700 nm region. The calculation reproduces the general profile and the position of the main absorption band near 670 nm, supporting the notion that the model captures key energy-absorption features of this complex.

Figure S11 compares the calculated LD spectrum with experimental data measured at 77 K[17]. The calculation broadly reproduces the lineshape of the dominant positive peak near 672 nm observed in the experimental spectrum. It is noted that a weaker positive feature around 683 nm present in the experimental trace is not captured in the simulation. This difference may reflect the fact that our calculation models the system at room temperature, whereas the experiment was conducted at 77 K. Lower temperatures can stabilize subtle conformational states or excitonic interactions that may be thermally averaged or less pronounced in our room-temperature model. The reproduction of the main LD feature suggests that the model provides a reasonable representation of the overall excited-state orientation properties within CP43.

The comparison between the calculated CD spectrum and the room-temperature experimental spectrum[17], presented in Fig. S12, reveals a discrepancy. The experimental spectrum displays a positive signal in the 650–673 nm range (with a peak near 668 nm) and switches to a negative signal in the 673–700 nm range, featuring two negative bands around 676 nm and 685 nm. In contrast, the calculated spectrum displays a largely inverted sign pattern across this region (negative in 650–673 nm and positive in 673–700 nm), yielding a single positive band near 678 nm. This outcome highlights the pronounced sensitivity of CD signals to chiral structural

details. While quantitative agreement is limited, the calculation still captures the overall alternating pattern of positive and negative signals within this spectral region.

The comparisons above demonstrate that the site energies and coupling terms employed in this study successfully reproduce the main features of the CP43 absorption and linear dichroism spectra.

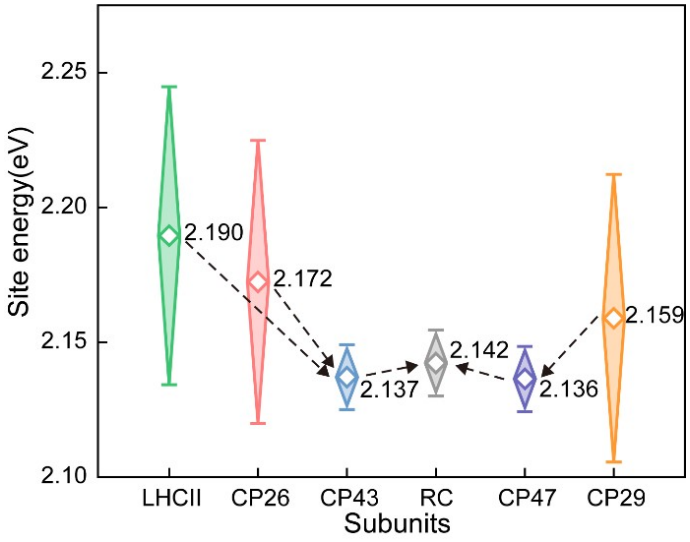

Fig. S1 Diamond box plots of site energies for in C_2S_2-type PSII-LHCII subunits derived from QM method. Hollow diamonds indicate mean values, with boxes representing standard deviations (SD). Subunits are color-coded: CP26 (red), CP29 (orange), LHCII (green), CP43 (blue), CP47 (purple), and the reaction center (RC, dark gray). Black dashed arrows illustrate proposed energy transfer pathways from the peripheral antenna (LHCII/CP24/CP29) through the inner antenna (CP43/CP47) to the RC.

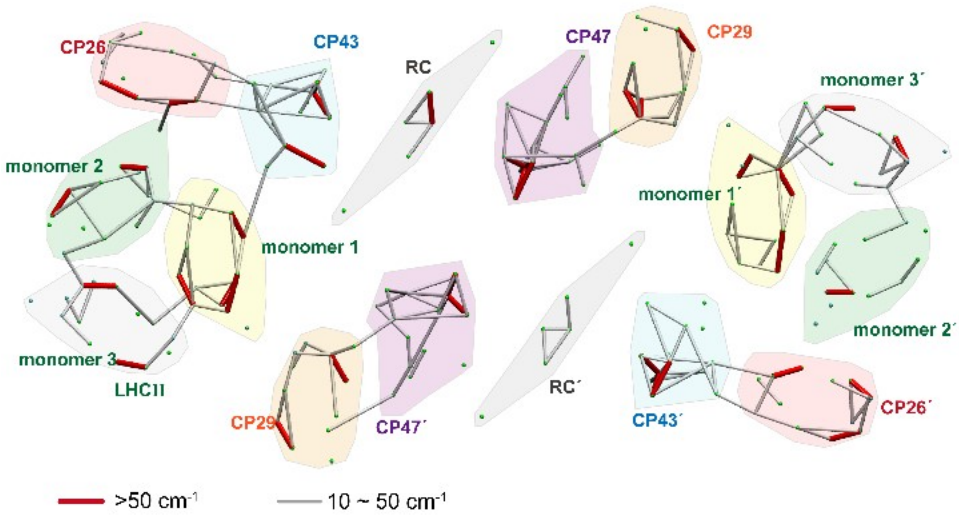

Fig. S2 Schematic diagram of the pigment coupling network in PSII-LHCII supercomplex. Inter-pigment couplings weaker than 10 cm^{-1} are omitted.

Tabel S1 Statistics of standard deviations of site energies for QM/MM and QM calculations on 206 pigment sites.

	QM/MM	QM
Mean of Standard Deviation	0.014	0.013
Maximum of Standard Deviation	0.026	0.023
Minimum of Standard Deviation	0.005	0.005

Tabel S2 Statistical results of site energy of Chl a in each subunit of C_2S_2-type PSII-LHCII.

Protein	Average site energy(eV)	SD
LHCII trimer	2.147	0.0136
CP29	2.140	0.0080
CP26	2.145	0.0171
CP47	2.132	0.0158
CP43	2.136	0.0117
RC	2.141	0.0231

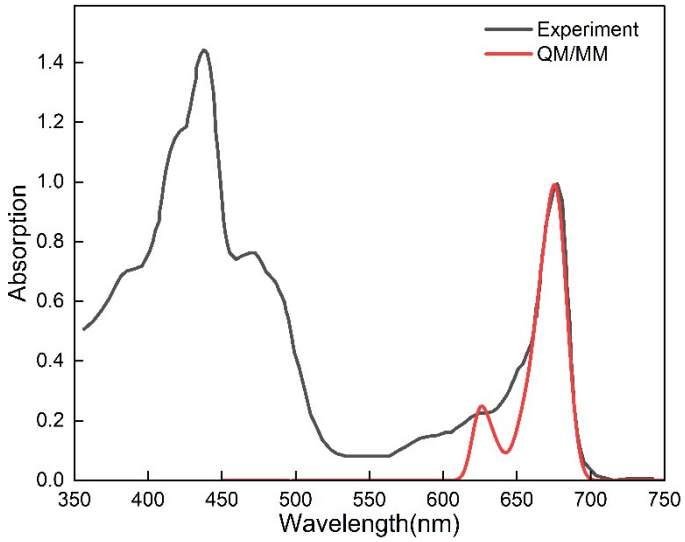

Fig. S3 Comparison of QM/MM-based absorption spectra of the PSII-LHCII supercomplex with experimental spectra at room temperature. Absorption spectra of the PSII-LHCII supercomplex calculated using QM/MM (CAM-B3LYP method) are compared with experimental spectra measured at room temperature[2]. To match the position of the Chl a experimental peak, the site energies in the QM/MM calculations were shifted to lower energies by 0.0285 eV[1].

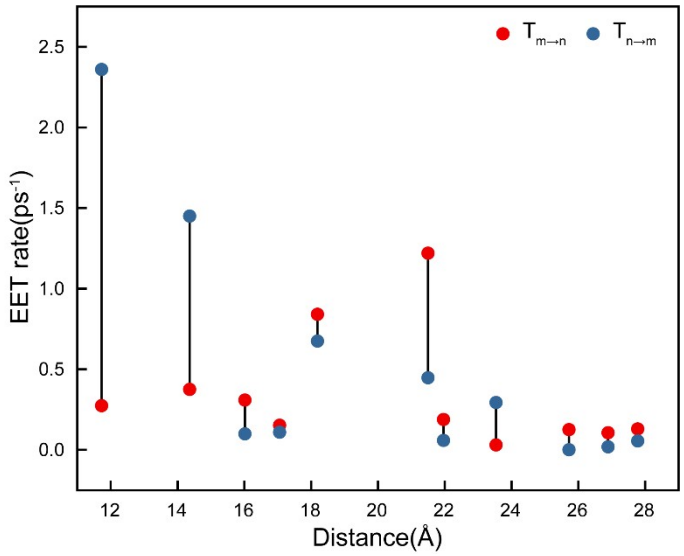

Fig. S4 Pigment Distances and Energy Transfer Rates for Key Pathways. The scatter plot shows the Mg-Mg distances (Å) versus energy transfer rates (ps^{-1}) for key donor-acceptor pairs. The red and blue data points represent the forward and backward transfer rates for the same pigment pair, respectively.

Table S3 Distances and energy transfer rates for key EET pathways from peripheral to inner antennas.

Donor	Receptor	d(Å)	$T_{m\to n}$ (ps^{-1})	$T_{n\to m}$ (ps^{-1})
$a611_{CP26}$	$a512_{CP43}$	18.19	0.84	0.68
$a612_{CP26}$	$a512_{CP43}$	25.72	0.13	0.00
$a613_{CP26}$	$a512_{CP43}$	26.89	0.11	0.02
$a614_{CP26}$	$a503_{CP43}$	16.02	0.31	0.10
$a613_{CP29}$	$a602_{CP47}$	21.96	0.19	0.06
$a616_{CP29}$	$a616_{CP47}$	14.36	0.38	1.45
$a603_{CP29}$	$a616_{CP47}$	23.54	0.03	0.29
$a611_{M1}$	$a506_{CP43}$	17.06	0.15	0.11
$a612_{M1}$	$a506_{CP43}$	21.50	1.22	0.45
$a613_{M1}$	$a506_{CP43}$	27.78	0.13	0.06
$b601_{M1}$	$b609_{M2}$	11.73	0.27	2.36

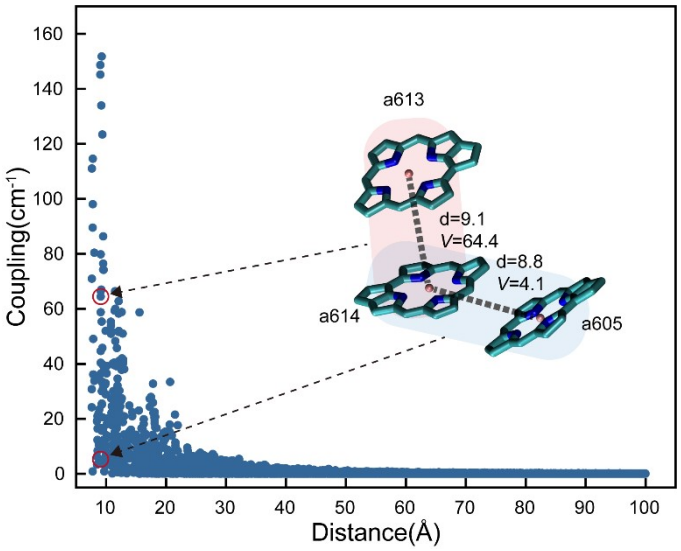

Fig. S5 Coupling strength versus inter-pigment distance. The scatter plot depicts the decay of electronic coupling (|V|) with increasing Mg-Mg distance for all pigment pairs within 100 Å. The embedded structural view highlights the chlorophylls a605, a613, and a614 in CP43, exemplifying how relative orientation, in addition to distance, determines the coupling strength between closely spaced pigments.

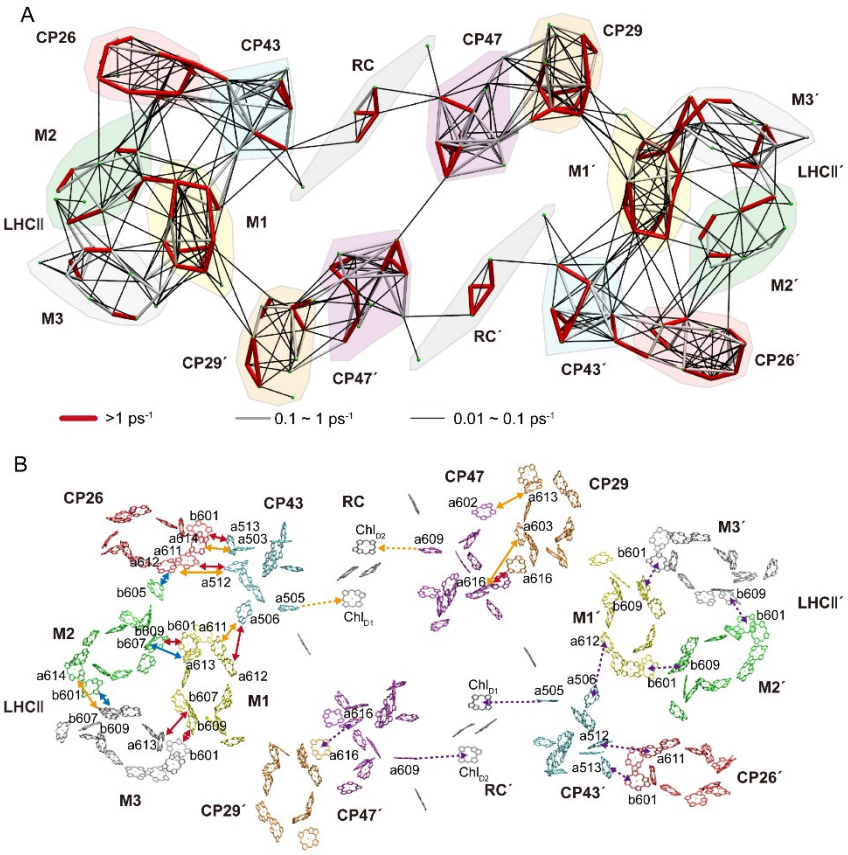

Fig. S6 FRET network and excitation energy transfer (EET) pathways under equalized site energies in PSII-LHCII supercomplex. (A) The map of inter-pigment EET rates calculated under the condition of equal site energies for all pigments. Inter-pigment rates slower than 0.01 ps^{-1} are omitted. (B) EET connections between the pigments are visualized from the stromal side, with time constants (τ, ps) indicated by arrows. Due to the absence of an energy gradient, EET connections are bidirectional. EET connections are indicated by solid arrows categorized by time constants: red arrows denote $\tau < 2$ ps, blue arrows represent $2 \leq \tau < 5$ ps, and orange arrows signify $5 \leq \tau \leq 10$ ps. Inner antenna to RC transfers are shown as orange dashed arrows. The fastest EET pathways between subunits are indicated by a purple dotted arrow in monomer 2. The displayed time constants (τ, ps) represent the inverse of the energy transfer rates ($\tau = 1/T_{m \to n}$, in ps).

Table S4 Inter-pigment (pairwise) energy transfer times across antenna interfaces obtained from multiscale simulation and a model with equal site energies.

Donor	Receptor	EET Time (ps)[1]	
		System 1[2]	System 2[3]
$b601_{CP26}$	$a513_{CP43}$	-	0.8(0.8)
$a611_{CP26}$	$a512_{CP43}$	1.2(1.5)	1.3(1.3)
$a612_{CP26}$	$a512_{CP43}$	7.9	9.8(9.8)
$a613_{CP26}$	$a512_{CP43}$	9.4	-
$a614_{CP26}$	$a503_{CP43}$	3.2	5.0(5.0)
$a613_{CP29}$	$a602_{CP47}$	5.3	8.3(8.3)
$a616_{CP29}$	$a616_{CP47}$	2.7(0.7)	1.1(1.1)
$a603_{CP29}$	$a616_{CP47}$	(3.4)	6.3(6.3)
$a611_{M1}$	$a506_{CP43}$	6.5(9.1)	7.6(7.6)
$a612_{M1}$	$a506_{CP43}$	0.8(2.2)	1.2(1.2)
$a613_{M1}$	$a506_{CP43}$	7.7	-
$b609_{M2}$	$b601_{M1}$	0.4(3.6)	0.8(0.8)
$b607_{M2}$	$a613_{M1}$	-	4.6(4.6)
$b609_{M1}$	$b601_{M3}$	1.2(1.2)	1.2(1.2)
$b607_{M1}$	$a613_{M3}$	-	1.7(1.7)
$b609_{M3}$	$b601_{M2}$	2.4	4.5(4.5)
$a603_{M3}$	$a602_{M2}$	(9.1)	-
$b607_{M3}$	$a614_{M2}$	-	9.1(9.1)
$b605_{M2}$	$a612_{CP26}$	-	3.0(3.0)
$a505_{CP43}$	Chl_{D1}	38.8(29.6)	33.7(33.7)
$a609_{CP47}$	Chl_{D2}	16.9	12.9(12.9)

[1] This table summarizes the energy transfer times for pathways between light-harvesting antennas (<10 ps) and the fastest pathways from inner antennas to the RC (<50 ps). Values in parentheses denote the reverse transfer time. Omitted entries indicate transfer times exceeding these thresholds.

[2] Data were obtained from the multiscale simulation protocol.

[3] Data were calculated under the condition of equal site energies for all pigments.

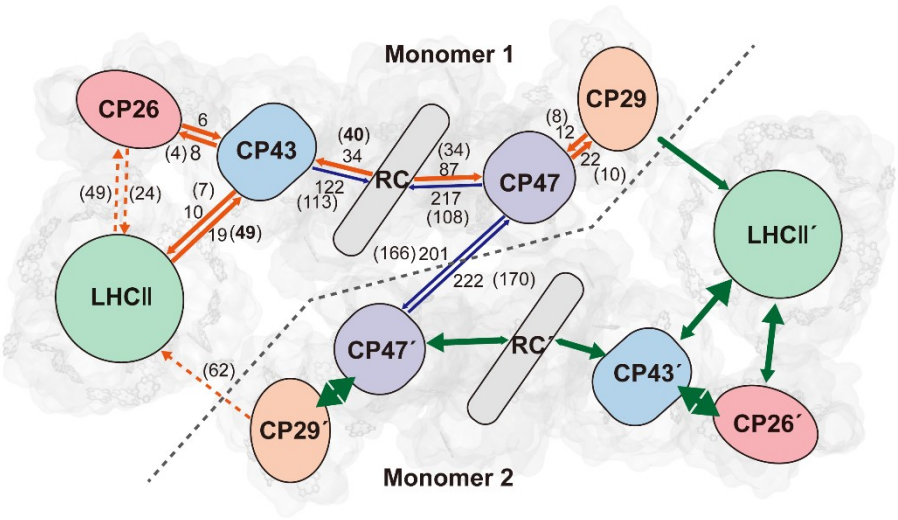

Fig. S7 Schematic diagram of excitation energy transfer pathways between subunits under equalized site energies. Pathways and time constants (τ, in ps) were calculated using generalized Förster theory. On the Monomer 1 side, energy transfer is indicated by solid arrows color-coded by time constant: orange for $\tau \leq 100$ ps and blue for $\tau \leq 250$ ps. Transfer between peripheral antennas is shown with dotted-line arrows. The time constants in the parentheses are calculated under the condition of consistent site energy. On the Monomer 2 side, inter-subunit energy transfer is represented by dark green double-headed arrows, with sizes proportional to the transfer rates. All time constants represent the inverse of the energy transfer rate ($\tau = 1/T_{m \to n}$).

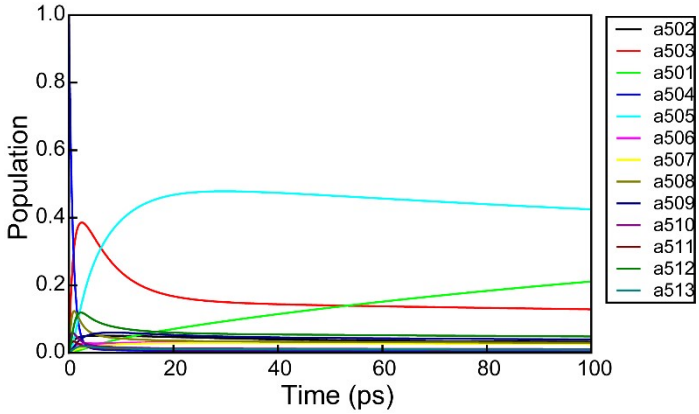

Fig. S8 Kinetics of excitation energy transfer of pigments in CP43. Kinetics of excitation energy transfer with the initial excitation site at a504 on the luminal side of CP43. Data were obtained from the multiscale simulation protocol.

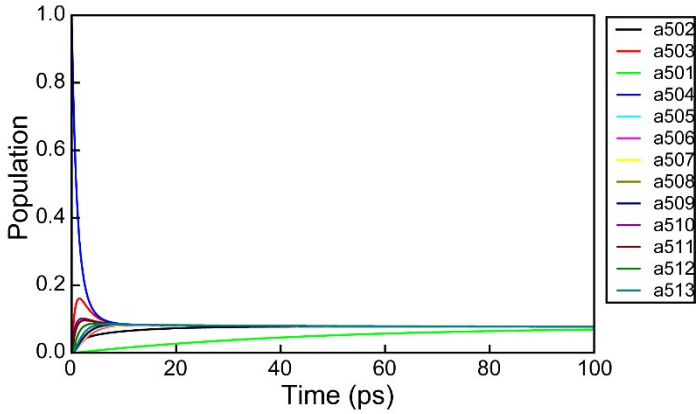

Fig. S9 Kinetics of excitation energy transfer of pigments in CP43. Kinetics of excitation energy transfer with the initial excitation site at a504 on the luminal side of CP43. Data were calculated under the condition of equal site energies for all pigments.

Table S5 Site energies (in eV) for RC from the present work and prior studies[4, 12].

Pigment	This study	Raszewski (2005)
P_{D1}	1.890	1.862
P_{D2}	1.863	1.862
Chl_{D1}	1.833	1.829
Chl_{D2}	1.829	1.859
$ChlZ_{D1}$	1.851	1.859
$ChlZ_{D2}$	1.870	1.856

Table S6 Site energies (in eV) for CP43 from the present work and prior studies[5].

Pigment	This study	Müh (2012)
a502	1.851	1.859
a503	1.840	1.846
a501	1.829	1.852
a504	1.868	1.830
a505	1.831	1.840
a506	1.853	1.859
a507	1.854	1.829
a508	1.852	1.845
a509	1.850	1.828
a510	1.860	1.877
a511	1.864	1.859
a512	1.848	1.854
a513	1.862	1.861

Table S7 Site energies (in eV) for CP47 from the present work and prior studies[3].

Pigment	This study	Raszewski (2008)
a602	1.837	1.821
a603	1.850	1.867
a604	1.850	1.834
a605	1.864	1.854
a606	1.847	1.836
a607	1.836	1.845
a608	1.851	1.876
a609	1.872	1.856
a610	1.822	1.836
a611	1.829	1.893
a612	1.846	1.824
a613	1.864	1.867
a614	1.833	1.842
a615	1.850	1.845
a616	1.872	1.856
a617	1.825	1.801

Table S8 Site energies (in eV) for LHCII from the present work and prior studies[14].

Pigment	This study	Novoderezhkin (2011)
b601	1.960	1.970
a602	1.871	1.879
a603	1.867	1.895
a604	1.856	1.917
b605	1.973	1.944
b606	1.965	1.965
b607	1.933	1.948
b608	1.974	1.954
b609	1.990	1.949
a610	1.867	1.869
a611	1.856	1.874
a612	1.861	1.871
a613	1.860	1.881
a614	1.847	1.892

Table S9 Site energies (in eV) for CP29 from the present work and prior studies[13, 15].

Pigment	This study	Müh (2014)	Mascoli (2020)
a601	1.841	-	1.887
a602	1.856	1.857	1.862
a603	1.854	1.847	1.862
a604	1.846	1.836	1.901
b606	1.965	1.945	1.999
b607	1.956	1.914	1.947
b608	1.962	1.914	1.987
a609	1.858	1.857	1.868
a610	1.861	1.850	1.869
a611	1.865	1.841	1.862
a612	1.859	1.847	1.873
a613	1.846	1.845	1.872
a616	1.862	-	-

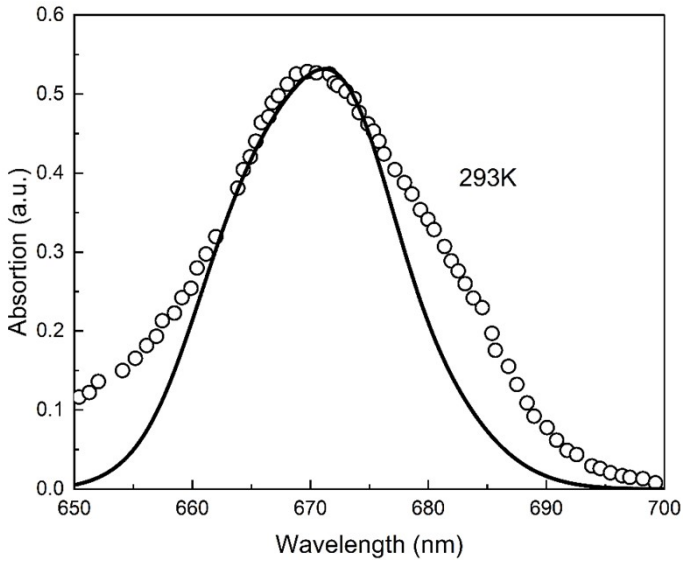

Fig. S10 Comparison of calculated and experimental absorption spectra of the CP43 subcomplex. The calculated spectrum (filled circles) is based on the TrEsp method for couplings and QM/MM-derived site energies (Table S6). The experimental spectrum (open circles) was recorded at 293 K[6].

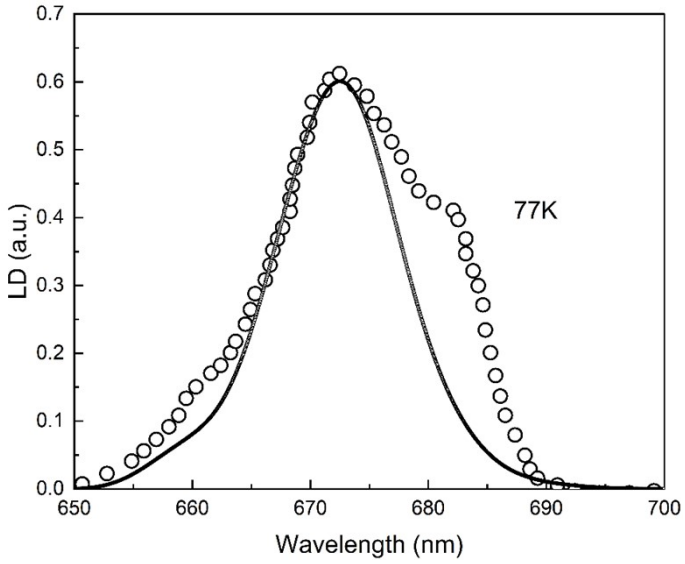

Fig. S11 Comparison of calculated and experimental linear dichroism (LD) spectra of the CP43 subcomplex. The calculated spectrum (filled circles) is based on the TrEsp method for couplings and QM/MM-derived site energies (Table S6). The experimental spectrum (open circles) was recorded at 77 K[17].

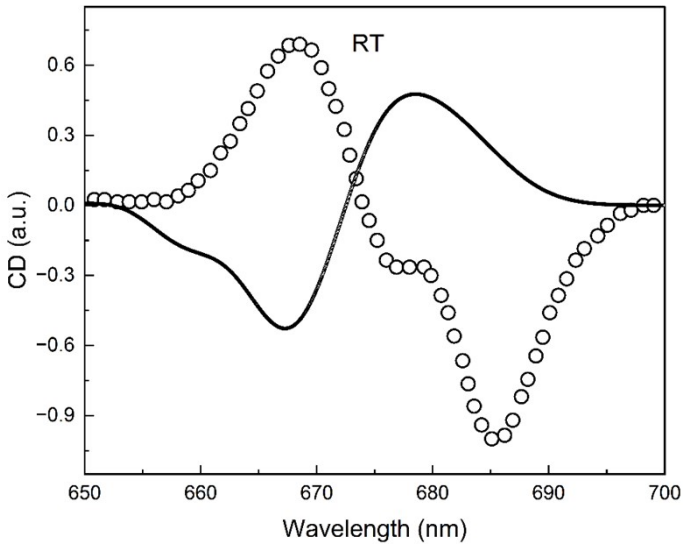

Fig. S12 Comparison of calculated and experimental circular dichroism (CD) spectra of the CP43 subcomplex. The calculated spectrum (filled circles) is based on the TrEsp method for couplings and QM/MM-derived site energies (Table S6). The experimental spectrum (open circles) was recorded at room temperature (RT)[17].

REFERENCES

1. S. Yin, M. G. Dahlbom, P. J. Canfield, N. S. Hush, R. Kobayashi and J. R. Reimers, *J. Phys. Chem. B*, 2007, **111**, 9923-9930.
2. X. Wei, X. Su, P. Cao, X. Liu, W. Chang, M. Li, X. Zhang and Z. Liu, *Nature*, 2016, **534**, 69-74.
3. G. Raszewski and T. Renger, *J. Am. Chem. Soc.*, 2008, **130**, 4431-4446.
4. G. Raszewski, W. Saenger and T. Renger, *J. Biol. Chem.*, 2005, **88**, 986-998.
5. F. Müh, M. E.-A. Madjet and T. Renger, *Photosyn. Res.*, 2012, **111**, 87-101.
6. F. Müh, M. Plöckinger, H. Ortmayer, M. Schmidt am Busch, D. Lindorfer, J. Adolphs and T. Renger, *J. Photochem. Photobiol. B.*, 2015, **152**, 286-300.
7. V. Novoderezhkin, J. M. Salverda, H. van Amerongen and R. van Grondelle, *J. Phys. Chem. B*, 2003, **107**, 1893-1912.
8. M. K. Sener, D. Lu, T. Ritz, S. Park, P. Fromme and K. Schulten, *J. Phys. Chem. B*, 2002, **106**, 7948-7960.
9. C. Kreisbeck and A. Aspuru-Guzik, *Chem. Sci.*, 2016, **7**, 4174-4183.
10. S. Yang, Jr., D. J. Wales, E. J. Woods and G. R. Fleming, *Nat. Commun.*, 2024, **15**, 8763.
11. D. I. G. Bennett, K. Amarnath and G. R. Fleming, *J. Am. Chem. Soc.*, 2013, **135**, 9164-9173.
12. G. Raszewski, B. A. Diner, E. Schlodder and T. Renger, *J. Biol. Chem.*, 2008, **95**, 105-119.
13. V. Mascoli, V. Novoderezhkin, N. Liguori, P. Xu and R. Croce, *BBA-Bioenergetics*, 2020, **1861**, 148156.
14. V. Novoderezhkin, A. Marin and R. Van Grondelle, *Phys. Chem. Chem. Phys.*, 2011, **13**, 17093-17103.
15. F. Müh, D. Lindorfer, M. Schmidt Am Busch and T. Renger, *Phys. Chem. Chem. Phys.*, 2014, **16**, 11848-11863.
16. K. Saito, K. Mitsuhashi, H. Tamura and H. Ishikita, *J. Biol. Chem.*, 2023, **122**, 470-483.
17. M.-L. Groot, R. N. Frese, F. L. de Weerd, K. Bromek, Å. Pettersson, E. J. G. Peterman, I. H. M. van Stokkum, R. van Grondelle and J. P. Dekker, *J. Biol. Chem.*, 1999, **77**, 3328-3340.